

Multistability in rotating spherical shell convection

F. Feudel and N. Seehafer

Institut für Physik und Astronomie, Universität Potsdam, Karl-Liebknecht-Strasse 24/25, 14476 Potsdam, Germany

L. S. Tuckerman

PMMH (UMR 7636 CNRS-ESPCI-UPMC Paris 6-UPD Paris 7), 10 rue Vauquelin, 75005 Paris, France

M. Gellert

Leibniz-Institut für Astrophysik Potsdam, An der Sternwarte 16, 14482 Potsdam, Germany

(Received 8 November 2012; published 27 February 2013)

The multiplicity of stable convection patterns in a rotating spherical fluid shell heated from the inner boundary and driven by a central gravity field is presented. These solution branches that arise as rotating waves (RWs) are traced for varying Rayleigh number while their symmetry, stability, and bifurcations are studied. At increased Rayleigh numbers all the RWs undergo transitions to modulated rotating waves (MRWs) which are classified by their spatiotemporal symmetry. The generation of a third frequency for some of the MRWs is accompanied by a further loss of symmetry. Eventually a variety of MRWs, three-frequency solutions, and chaotic saddles and attractors control the dynamics for higher Rayleigh numbers.

DOI: [10.1103/PhysRevE.87.023021](https://doi.org/10.1103/PhysRevE.87.023021)

PACS number(s): 47.55.P-, 47.32.Ef, 47.20.Ky, 47.54.-r

I. INTRODUCTION

Buoyancy-driven convection in a rotating spherical fluid shell which is heated, either by internal heat sources or by imposing a temperature gradient between the spherical boundaries, and is subject to a central gravity field represents an idealized model for fluid flows in various geophysical and astrophysical bodies, such as the outer cores of the terrestrial planets, the envelopes of the giant planets, or the convection zone of the Sun. Its study has a long history which began with linear stability analyses [1–3] and was continued by the investigation of pattern formation beyond the onset of convection [4–6]. Although this idealized model is a rather rough attempt at explaining the complex processes occurring in geophysical and astrophysical applications, it describes some basic generic features and can also be observed in more comprehensive models. Its solutions have been studied over a wide range of the control parameters, with the results reported in a large number of publications, but not all details of the bifurcations and features of the different solution branches are fully understood yet.

The present study was initiated by a numerical dynamo benchmark test [7] that we carried out using a spectral code developed by Hollerbach [8]. The results obtained with the code passed all requirements of the test with a high accuracy concerning both the magnetohydrodynamical and purely convective phenomena. Our investigations also yielded a variety of additional solutions and further properties of known solutions in the parameter range prescribed for the benchmark test. Concentrating on purely convective phenomena, we studied symmetry-breaking bifurcations in the nonrotating sphere [9]. The present study extends our investigation to the rotating case. We examine the dynamics of coexisting time-dependent solution branches and their properties in a selected small parameter range. In particular, these states can be interpreted as rotating waves (RWs) and modulated rotating waves (MRWs) and their generation can be connected to the azimuthal circle

symmetry of the problem. The spatiotemporal symmetry of the solutions is one focus of our investigation.

The paper is organized as follows: In Sec. II we introduce the model and describe the numerics used. Then, in Sec. III, the primary convective states, the RWs, are studied, followed by an investigation of the MRWs, which bifurcate from the RWs, in Sec. IV. Higher-frequency and chaotic dynamics are the subject of Sec. V, and finally, in Sec. VI, we discuss our results.

II. BASIC EQUATIONS AND NUMERICS

We study classical Rayleigh-Bénard convection in a spherical fluid shell rotating with constant angular velocity $\boldsymbol{\Omega} = \Omega \mathbf{e}_z$ about the z axis (\mathbf{e}_z is the unit vector in the z direction). The shell is heated from within by imposing a temperature difference ΔT between the inner and outer boundaries. Using the Boussinesq approximation, the governing equations are made nondimensional with the gap size d as the unit of length, so that the dimensionless outer and inner radii are r_o and $r_i = r_o - 1$, respectively. Time is scaled by the viscous diffusion time d^2/ν , where ν is the kinematic viscosity. The flow velocity \mathbf{u} is scaled by the viscous diffusion velocity ν/d , temperature by ΔT , and pressure p by $\rho_o \nu \Omega$, where ρ_o is the reference mass density at the reference temperature T_o . The gravitational acceleration \mathbf{g} is assumed to be proportional to the distance \mathbf{r} from the center of the sphere (as valid for the self-gravity in the interior of a spherical body with constant mass density) and is thus expressible in the form $\mathbf{g} = -(g_o/r_o)\mathbf{r}$, where g_o is the absolute value of \mathbf{g} at radius r_o . The resulting nondimensional equations read

$$\text{Ek} \left[\frac{\partial \mathbf{u}}{\partial t} + (\mathbf{u} \cdot \nabla) \mathbf{u} - \nabla^2 \mathbf{u} \right] = -\nabla p + \text{Ra} T \frac{\mathbf{r}}{r_o} - 2 \mathbf{e}_z \times \mathbf{u}, \quad (1a)$$

$$\frac{\partial T}{\partial t} + \mathbf{u} \cdot \nabla T = \frac{1}{\text{Pr}} \nabla^2 T, \quad (1b)$$

$$\nabla \cdot \mathbf{u} = 0, \quad (1c)$$

where

$$\text{Ek} = \frac{\nu}{d^2\Omega}, \quad \text{Ra} = \frac{\alpha \Delta T g_o d}{\Omega \nu}, \quad \text{Pr} = \frac{\nu}{\kappa} \quad (2)$$

are the Ekman number, a modified Rayleigh number (α is the thermal expansion coefficient), and the Prandtl number (κ is the thermal diffusivity). The centrifugal acceleration and a gradient part of the acceleration due to buoyancy have been included in the pressure gradient on the right-hand side of Eq. (1a). Ra is connected with the conventional Rayleigh number $\tilde{\text{Ra}}$ by the relation $\text{Ra} = \tilde{\text{Ra}}\text{Ek}/\text{Pr}$.

The system is characterized by four dimensionless parameters, namely, the three numbers defined in Eq. (2) and the outer radius r_o (or, equivalently, the aspect ratio $\eta = r_i/r_o$). In our choice of these parameters we follow the benchmark study [7]: $r_o = 20/13$ (so that $r_i = r_o - 1 = 7/13$ and $\eta = 7/20$), $\text{Pr} = 1$ and $\text{Ek} = 10^{-3}$ (corresponding to a Taylor number $\text{Ta} = 4/\text{Ek}^2 = 4 \times 10^6$). Ra remains a free control parameter.

The boundary conditions imposed at the spherical surfaces are those corresponding to rigid and thermally perfectly conducting spheres, namely,

$$\mathbf{u} = \mathbf{0} \quad \text{at } r_i, r_o, \quad (3a)$$

$$T = 1 \quad \text{at } r = r_i \quad \text{and} \quad T = 0 \quad \text{at } r = r_o, \quad (3b)$$

with the associated temperature profile in the time-independent conductive basic state being given by

$$T_c(r) = \frac{r_o r_i}{r} - r_i. \quad (4)$$

Due to the presence of the Coriolis force [the last term on the right-hand side of Eq. (1a)], the full spherical symmetry of the nonrotating case is broken. Equations (1a)–(1c) remain equivariant with respect to the symmetry group $\text{SO}(2) \times \text{Z}_2$, generated by rotations about the z axis [forming the special orthogonal group $\text{SO}(2)$, which is isomorphic to the circle group S^1] and reflections in the equatorial plane (forming the reflection group Z_2). This symmetry plays a determining role in the transitions between different solutions.

The computations were carried out by means of a spectral solver [8] which makes use of the representation of the velocity field by toroidal and poloidal potentials:

$$\mathbf{u}(r, \theta, \varphi, t) = \nabla \times f^{\text{tor}} \mathbf{e}_r + \nabla \times \nabla \times f^{\text{pol}} \mathbf{e}_r. \quad (5)$$

All variables, in particular the potentials f^{tor} and f^{pol} and the temperature T , are expanded in terms of spherical harmonics Y_ℓ^m for the angular dependence and Chebyshev polynomials T_k for the radial dependence:

$$f(r, \theta, \varphi, t) = \sum_{k, \ell, m} T_k \left(\frac{2r - (r_o + r_i)}{r_o - r_i} \right) P_\ell^m(\cos \theta) \times [f_{k\ell m}(t)e^{im\varphi} + f_{k\ell m}^*(t)e^{-im\varphi}] \quad (6)$$

(a superscript asterisk denotes the complex conjugate). The time stepping is based on a modified Crank-Nicolson algorithm for the diffusive terms and a Runge-Kutta scheme for the remaining terms. A spatial resolution of (30,40,40) in (r, θ, φ) and a time step of $\Delta t = 10^{-4}$ are used.

For demonstrating some of the dynamical features of our system we use the total kinetic energy of the fluid,

$$E_{\text{kin}} = \frac{1}{2} \int_V \mathbf{u}^2 d^3r, \quad (7)$$

with V denoting the spherical shell.

III. ROTATING WAVES

For low Rayleigh numbers and all rotation rates, the pure heat conduction state with the fluid at rest and the temperature profile T_c , given by Eq. (4), is the only stable solution. At a Rayleigh number $\text{Ra} > 55.9$, this basic state loses stability in a supercritical Hopf bifurcation where the azimuthal mode $m = 4$ becomes unstable. The theory of bifurcations with symmetry predicts that if the bifurcation from the basic state breaks the azimuthal symmetry, this bifurcation is generically a Hopf bifurcation that generates rotating waves drifting along the group orbit [10–12]. RWs are stationary solutions in a suitably rotating coordinate frame, and accordingly they are also called relative equilibria. In our case the RWs show an azimuthal cyclic Z_4 symmetry. The solution branch is correspondingly denoted by RW4.

In order to find additional solutions, numerous simulations with different initial conditions at various Rayleigh numbers were carried out, which led to three further branches of RWs. More precisely, a stable RW with a Z_5 symmetry with respect to azimuthal rotations appears in a simulation at $\text{Ra} = 100$ by taking the conductive state as the initial condition. In addition, a magnetic RW branch with a Z_3 symmetry was already known from previous dynamo simulations, a topic which is not covered in this article. By switching off the coupling to the magnetic field the attractor is reduced to a pure convective RW state with a Z_3 symmetry. Finally, a fourth branch was found by taking a superposition of the Z_4 and Z_5 states as an initial condition for a simulation. This gave a RW attractor with Z_2 symmetry. In accordance with their symmetry properties these RW branches are denoted by RW5, RW3, and RW2, respectively.

Contour plots of the radial velocity in the middle of the spherical gap and in the equatorial plane are exhibited in Figs. 1 and 2 for $\text{Ra} = 100$, the value of the Rayleigh number used in the previously mentioned benchmark study [7]. The kinetic energy and precession frequency of RW4 agree with the benchmark values. The existence of the additional RW5, RW3, and RW2 solutions manifests the feature of multistability of RWs over a large interval of the Rayleigh number. All RWs are spatially invariant under reflections in the equatorial plane, i.e., the original Z_2 symmetry is not broken.

Although nonlinear interactions generate higher harmonics as Ra is increased, the fundamental azimuthal mode (e.g., that with mode number $m = 4$ for the branch RW4) continues to be the dominant one, followed by the $m = 0$ mode, which gives the mean flow (that is, differential rotation and meridional circulation). The $m = 0$ mode amplitude is constant. For $m \neq 0$, the real and imaginary parts oscillate while leaving the absolute value constant.

We have found empirically that at least the RW4, RW5, and RW3 branches can generate magnetic fields (provided the

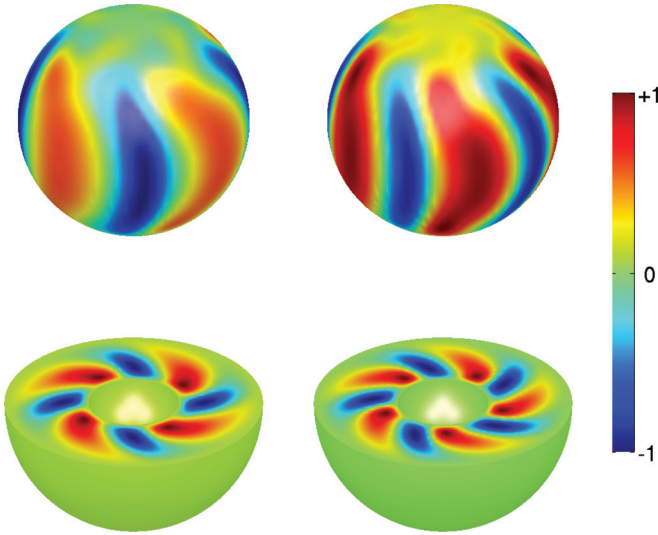


FIG. 1. (Color online) Time-asymptotic states of RW4 (left) and RW5 (right) at $Ra = 100$. Depicted is the radial velocity normalized to its maximum modulus at midgap (upper row) and in the equatorial plane (lower row). Positive values (red) correspond to upwelling and negative values (blue) to downwelling flows.

fluid is electrically conducting), but we leave this property to future studies.

Figure 3 shows the kinetic energy of the RWs for a dense set of Rayleigh numbers, obtained as time-asymptotic states by long-time simulations.

The RW3 and RW5 branches originate at Rayleigh numbers higher than that of the RW4 branch. Hence, these two branches must be unstable when they bifurcate from the conductive state, but are stabilized by subsequent bifurcations at Rayleigh numbers $Ra = 60$ (RW3) and $Ra = 65$ (RW5). The lower limit ($Ra = 90$) of the RW2 branch is considerably higher than that of the other branches. This lower limit is marked by a subcritical oscillatory instability, below which the trajectory jumps onto the RW4 branch.

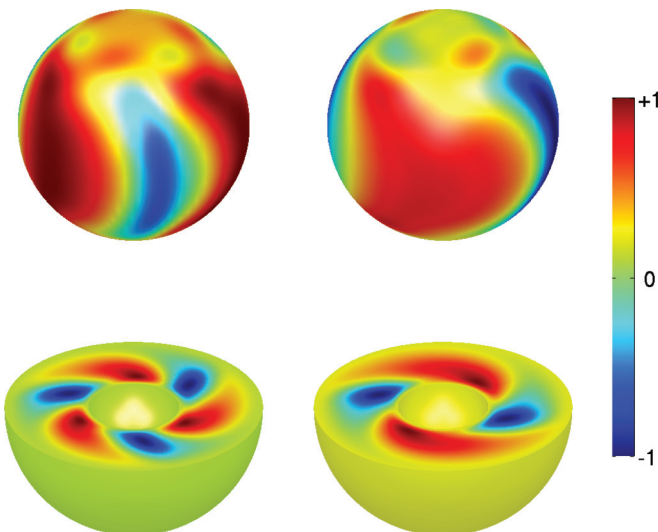


FIG. 2. (Color online) As Fig. 1 for RW3 (left) and RW2 (right).

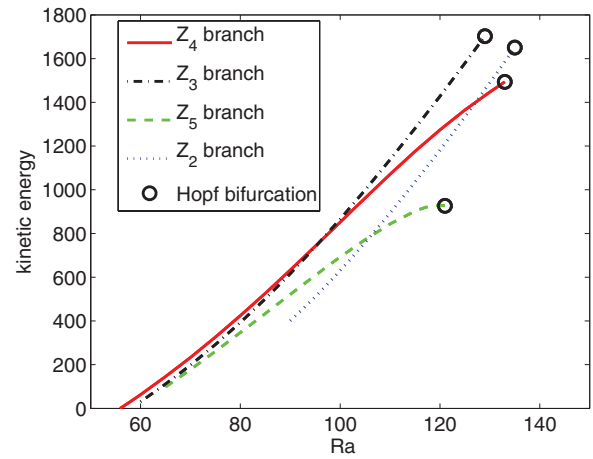


FIG. 3. (Color online) Bifurcation diagram exhibiting the kinetic energy of stable RWs vs. Ra .

Figure 4 depicts the precession frequency ω_{pr} of RWs as a function of the Rayleigh number; ω_{pr} is positive for prograde precession. At the onset of convection the RWs show a prograde precession. With increasing Rayleigh number the precession slows down and finally a retrograde precession takes place. We note that all RWs show the same linear scaling behavior over nearly the whole Rayleigh number interval of their stability. This is in agreement with the theory of Ecke *et al.* [12] which predicts a linear relation between the precession frequency ω_{pr} and the Rayleigh number. Here, however, we see two extensions of the theory of Ecke *et al.* [12]. Surprisingly, all of the lines in Fig. 4 have the same slope, independent of the fundamental azimuthal mode number m . Second, the dependence of frequency on Ra is linear in a range which is considerably above onset.

We can compare the precession of RWs in our system with that in other configurations combining rotation and convection. Depending on the rotation rate and the Prandtl number, the precession of RWs can be prograde or retrograde with respect to the overall system rotation [13]. In addition, convective structures can be more or less localized near inner or outer

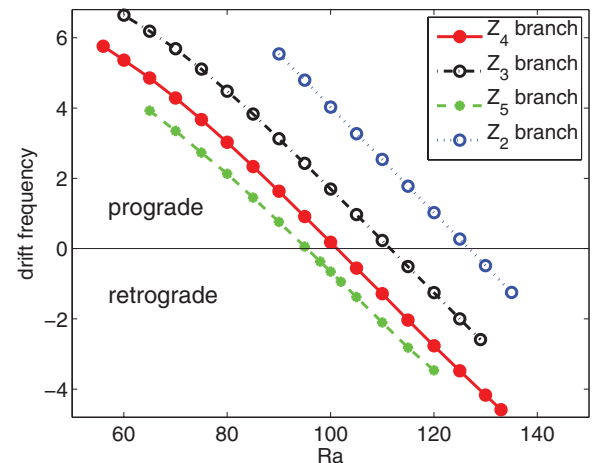


FIG. 4. (Color online) Drift frequency ω_{pr} of RWs vs Rayleigh number over the range of stability.

boundaries, with those at the outer boundaries usually called wall modes.

In Rayleigh-Bénard convection in a rotating circular cylinder, wall modes set in first if the rotation is rapid and in this case, a retrograde drift is observed [14]. This is also the case for rotating convection in an annulus [15,16], but other modes, which appear at higher Rayleigh numbers and are attached to the inner boundary, precess in the prograde direction.

In our spherical case, convection near onset takes the form of broad columnar vortices that are somewhat closer to the inner than to the outer boundary and which precess in the prograde direction. As the Rayleigh number is increased, the columnar vortices widen towards the outer wall and the precession becomes retrograde. Indeed, the results in [13] indicate that, at least at onset, the dominance of columnar over outer-wall-attached convection may favor prograde compared to retrograde drift, and vice versa, which would be in accordance with our observation of prograde precession. However, this issue is not yet well understood. We note that a similar reversal of the precession direction from prograde to retrograde in rotating spherical shell convection was reported by Kimura *et al.* [17].

For further increased Rayleigh number, eventually each of the RWs loses stability via a Hopf bifurcation (cf. Fig. 3) in which solution branches of modulated rotating waves are generated, whose properties are the subject of Sec. IV.

IV. TRANSITIONS TO MODULATED ROTATING WAVES

There exists a general mathematical theory for the classification of solutions created at secondary Hopf bifurcations of RWs [11,18]. These solutions appear as simply time periodic in coordinate frames moving with the speed of the corresponding wave, that is, in the frames rotating with angular velocity $1/Ek + \omega_{pr}$ with respect to the inertial rest frame. [We recall from Eq. (2) that $1/Ek$ is the dimensionless overall rotation rate of the system relative to the rest frame.] Here, we call these solutions MRWs, as is usual in physics; they are also called relative periodic orbits.

A well-known application of the theory concerns the transitions in the Taylor-Couette system, i.e., in the flow in the gap between differentially rotating coaxial circular cylinders. Based on the azimuthal $SO(2)$ equivariance of the governing equations, Rand [19] classified the possible MRWs. The solutions he predicted were found experimentally by Gorman and Swinney [20]; see also Gorman *et al.* [21]. Later, it was noticed that the ensemble of MRWs contains further solutions, whose presence can be explained if the system is modeled as having $SO(2) \times O(2)$ symmetry [azimuthal $SO(2)$ coupled with axial $O(2)$ symmetry] [22].

For our problem of rotating spherical Rayleigh-Bénard convection, the symmetry group is $SO(2) \times Z_2$ (see Sec. I). However, in the parameter range we have studied, the bifurcations are controlled by the $SO(2)$ subgroup only, since the Z_2 equatorial-plane reflection symmetry is preserved throughout all the solutions and transitions that we have studied. This Z_2 symmetry remains preserved even for the higher-frequency or chaotic states which are described later in Sec. V. Consequently, we can use the classification and notation given by Rand [19]. Another application of the theory

TABLE I. Characteristics of MRWs.

	Ra	ω_{pr}/ω_{mo}	\mathbf{I}_{MRW}	Interval of stability
MRW2	136	4.637/351.02	(2,1,1)	$136 \leq Ra \leq 148$
MRW3	130	2.369/380.80	(3,1,2)	$130 \leq Ra \leq 140$
MRW4	133.7	4.637/126.93	(4,2,1)	$133.5 < Ra < 133.8$
MRW5	122	4.025/12.62	(5,1,1)	$122 \leq Ra \leq 137.4$

is the flow in a circular cylinder driven by the rotation of an end wall [23], which also has only $SO(2)$ symmetry.

MRWs are quasiperiodic, i.e., characterized by two incommensurate frequencies ω_{pr} and ω_{mo} , with ω_{mo} denoting the frequency of a time-periodic modulation of the rotating waves. More specifically, there exists a basic time period τ , which we call the pattern-repeat period, after which, in the frame rotating with the wave, the pattern recovers its initial shape, but is azimuthally shifted. In general τ is different from both the precession and modulation periods. The kinetic energy and the Nusselt number, for instance, are time periodic with period τ . Rand [19] characterizes the MRWs by a triple of integers, $\mathbf{I}_{MRW} = (m, s, n)$. As before, m is the fundamental azimuthal wave number of the solution branch, or number of wave peaks. Although the azimuthal Z_m symmetry is broken (i.e., the different wave peaks of the MRWs oscillate with different phases), there remains an instantaneous Z_s symmetry, where s divides m . For example, s may be 1, 2, or 4 for $m = 4$, but can only be 1 or m for $m = 3$ or $m = 5$. The last element n of the triple $\mathbf{I}_{MRW} = (m, s, n)$ is such that the wave pattern at time $t + \tau$ in the reference frame rotating with angular velocity ω_{pr} differs from that at time t by a rotation through $2\pi n/m$, with $0 \leq n < m/s$. The modulation frequency $\omega_{mo} = 2\pi/\tau_{mo}$ is then given by the total period $\tau_{mo} = (m/s)\tau$ of the wave modulation.

In our case, all the RWs (see Fig. 3) lose their stability via secondary Hopf bifurcations at which the associated branches MRW2, MRW3, MRW4, and MRW5 of modulated rotating waves are generated. In the following we discuss the features of the MRWs at Rayleigh numbers slightly above their respective bifurcation points. Some characteristics are listed in Table I. The modulation frequencies in the second column of the table are nearly the same as the imaginary parts of the critical eigenvalues associated with the secondary Hopf bifurcations. For comparison, the rotation rate of the system relative to the rest frame is $1/Ek = 10^3$, where we recall that we use as our unit of time the viscous diffusion time across the gap.

The kinetic energies and Nusselt numbers oscillate with a single frequency ω_{mo} , as is the case for the $m = 0$ mode amplitudes. The modes with the fundamental azimuthal wave number are most strongly excited, followed by those with $m = 0$, as was the case for the RWs. All modes with $m \neq 0$ behave quasiperiodically with two incommensurate frequencies ω_{pr} and ω_{mo} .

Figures 5–7 show, for MRW5, MRW3, and MRW4, representative instantaneous profiles of the radial velocity as a function of azimuthal angle around the equator at the midgap. The selected times are multiples of the pattern-repeat period τ , and in each figure a full modulation period τ_{mo} is covered.

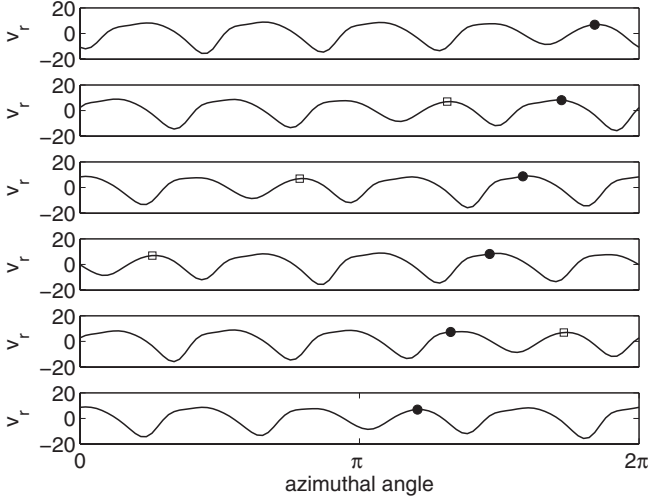


FIG. 5. Radial velocity v_r of MRW5 vs azimuthal angle φ around the equator at the midgap for $Ra = 122$ and $\mathbf{I}_{MRW} = (m,s,n) = (5,1,1)$. From top to bottom, times $t_j = t_0 + j\tau$ for $j = 0, \dots, 5$. Black dots, initially marking a selected wave crest, show the azimuthal drift, while squares indicate the reappearance of the wave crest at times t_j during the modulation cycle. (The squares are omitted when they would coincide with the black dots.)

In each panel of MRW3 and MRW5 (Figs. 5 and 6), it can be seen that each of the m oscillations differs from all the other ones. For MRW4, however, the two oscillations over $[0, \pi]$ are identical to the two oscillations over $[\pi, 2\pi]$; this is the manifestation of the value $s = 2$.

The drift, with angular velocity ω_{pr} with respect to that of the spherical boundaries, is retrograde or westwards (leftwards in the figures) in all three cases and is indicated by the slow wandering of black dots that initially mark a selected wave crest. After each time period τ the wave recovers its initial form, up to an azimuthal phase shift of $2\pi n/m + \omega_{pr}\tau$. This shift is indicated by hollow squares located on the selected wave crest (omitted in subfigures where they would

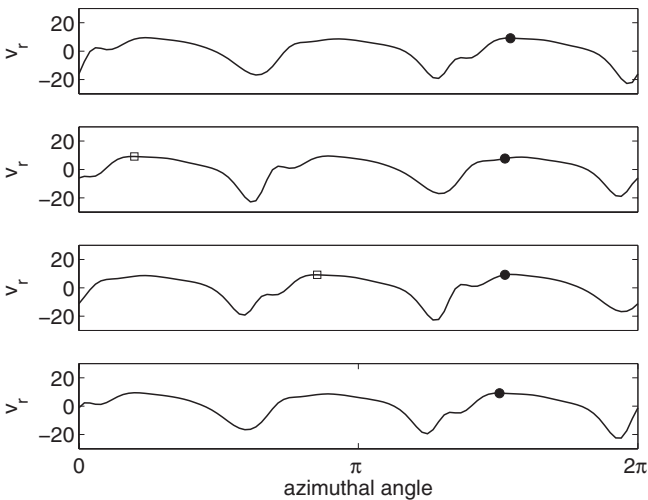


FIG. 6. As Fig. 5, but for MRW3 at $Ra = 130$, with $\mathbf{I}_{MRW} = (m,s,n) = (3,1,2)$, from top to bottom at times $t_j = t_0 + j\tau$ for $j = 0, \dots, 3$. The hollow square is displaced leftwards by two oscillations over each time τ , corresponding to the value $n = 2$.

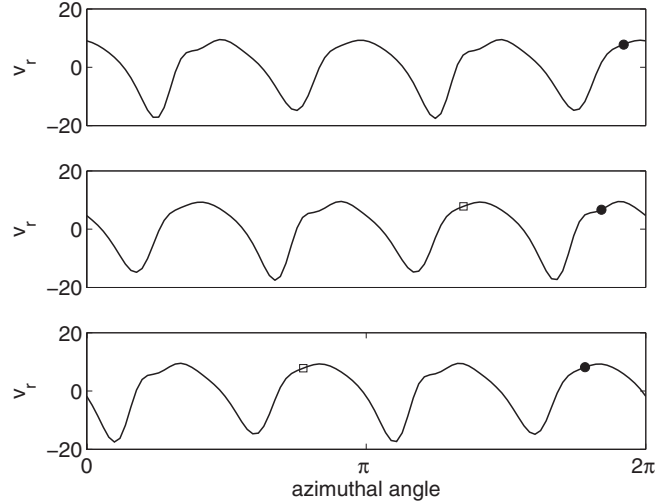


FIG. 7. As Fig. 5, but for MRW4 at $Ra = 133.7$, with $\mathbf{I}_{MRW} = (m,s,n) = (4,2,1)$, from top to bottom at times $t_j = t_0 + j\tau$ for $j = 0, 1, 2$. The wave form over $[\pi, 2\pi]$ is the same as that over $[0, \pi]$, corresponding to the value $s = 2$.

coincide with the black dots). These squares are displaced by n wavelengths after each time τ , i.e., by one wavelength for MRW5 (Fig. 5) and MRW4 (Fig. 7), both with $n = 1$, but by two wavelengths for MRW3, with $n = 2$. The state reached after the completion of the modulation cycle, depicted in the last panel of each figure, differs by an azimuthal shift of $\omega_{pr}\tau_{mo}$ from the initial state.

V. HIGHER-FREQUENCY AND CHAOTIC DYNAMICS

In this section we want to demonstrate multistability and the complexity of the dynamics for higher Rayleigh numbers where some of the modulated rotating waves have lost their stability. The MRW4 branch is stable only over a very small Rayleigh number interval (see Table I), and it is the first branch that undergoes a further Hopf bifurcation. By ramping up the Rayleigh number in small steps above this bifurcation point, we give an example of the qualitative changes that accompany the subsequent transitions between different solutions. Figure 8 shows, for three selected Rayleigh numbers, time series of the kinetic energy, presenting certain dynamical features along this route. In the top panel, at $Ra = 133.9$, the time series of the kinetic energy contains two dominant frequencies, which can be clearly identified in the corresponding power spectrum in Fig. 9 (left). Besides the pattern-repeat frequency $f_1 = 1/\tau$ of the original MRW4 branch, a second frequency f_2 appears. Thus, taking into account the precession frequency, a stable three-frequency solution has been formed (the precession does not change the kinetic energy and, hence, its frequency does not appear in the power spectrum). Quasiperiodic convection with two frequencies in addition to precession in a rotating spherical shell has previously been observed by Sun *et al.* [24].

It is not the aim of this study to elucidate all details in the transitions to aperiodic dynamics. However, we want to describe how the temporal behavior of the solutions is qualitatively changed by a further increase of the Rayleigh number. The time series of the kinetic energy shown in

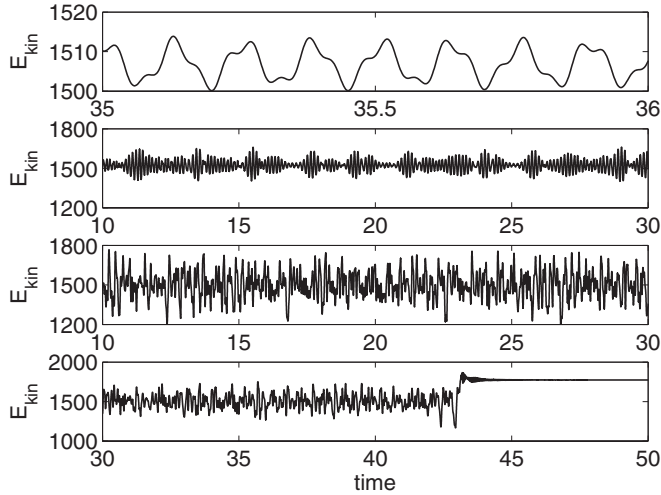


FIG. 8. Kinetic energy vs time at Rayleigh numbers above the instability point of MRW4, from top to bottom at $Ra = 133.9$, 135.0 , 135.2 , and 135.2 continued.

the three upper panels of Fig. 8 in conjunction with the corresponding power spectra in Fig. 9 reveal such qualitative changes. In the process, the three-frequency solution loses its regular quasiperiodicity and the temporal behavior becomes increasingly aperiodic. At $Ra = 135$, the time series of the kinetic energy shown in Fig. 8 (second panel from the top) is characterized by remnants of the quasiperiodic dynamics, interrupted by larger fluctuations. The corresponding power spectrum in Fig. 9 (middle) shows a broadening of the peaks at the two dominant frequencies, combined with an enhancement of the background noise.

A further ramping up of the Rayleigh number by a small step to $Ra = 135.2$ changes the temporal behavior drastically; see Fig. 8 (third panel from top). The behavior is now obviously strongly chaotic. The two originally dominant frequencies are embedded in a broadband spectrum whose exponential

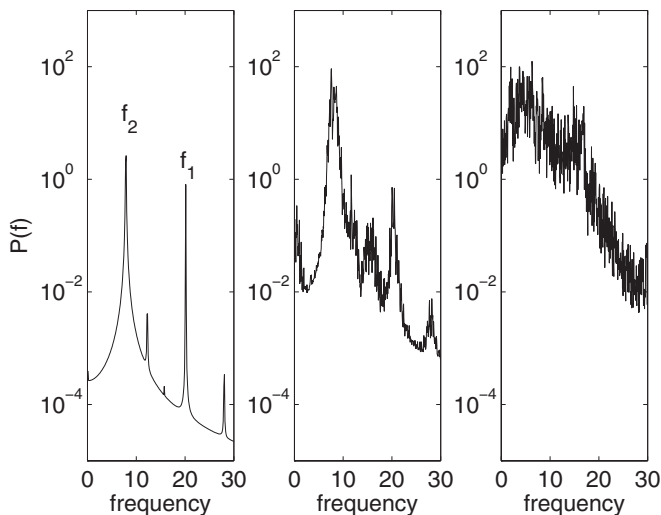


FIG. 9. Power spectrum $P(f)$ of kinetic energy for time-asymptotic states at $Ra = 133.9$ (left), $Ra = 135$ (middle), and $Ra = 135.2$ (right) on continuation of the branch MRW4.

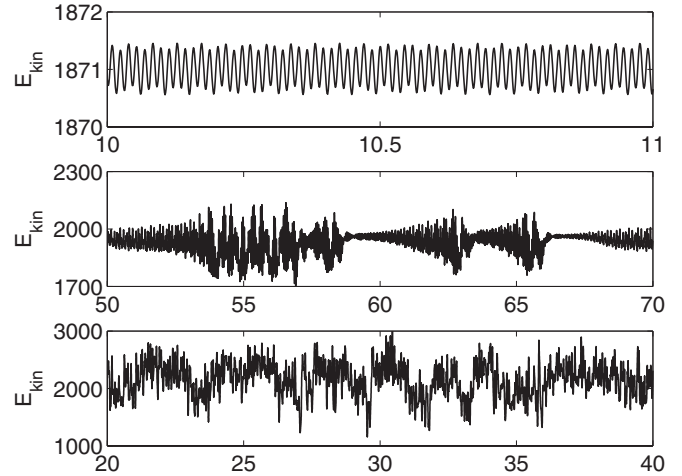


FIG. 10. Kinetic energy vs time at Rayleigh numbers above the instability point of MRW3, from top to bottom at $Ra = 141$, 145 , and 165 .

decay over the frequency range indicates the occurrence of deterministic chaos; see Fig. 9 (right).

Surprisingly, the chaos does not persist. After a longer simulation time the trajectory suddenly jumps to another, regular attractor, which can be identified as the MRW3 branch. This behavior is depicted in the bottom panel of Fig. 8 (a continuation in time of the panel above it). The resulting regular oscillations of the kinetic energy on the MRW3 branch are very small compared to the previous chaotic fluctuations and are not discernible in the figure (but are well resolved in the numerical computations).

We find transient chaos to be typical when starting from states in the modulated wave regime and ramping up the Rayleigh number above critical values at which the behavior is no longer strictly quasiperiodic, that is, to $Ra > 133.8$ for the MRW4 branch and to $Ra > 137.4$ for the MRW5 branch (Table I, right column). The resulting dynamics are controlled by long-lasting chaotic transients, where in most cases the trajectory eventually jumps to one of the coexisting regular attractors, namely, MRW2 or MRW3. The most convincing explanation for this unpredictable behavior is the presence of a chaotic saddle. In some cases (for instance, for $Ra = 135.5$, when starting with the same initial state as for simulating the time series at $Ra = 135.2$ on the prolonged MRW4 branch discussed above), we also observe seemingly persistent chaos over a simulation period of 100 viscous time units, but no final conclusion can be drawn here.

The results described raise the question of whether and if so, in what way, persistent chaos appears. In order to answer this question, the MRW3 branch, which had proved to be attractive for the quasichaotic solutions on the continuation of the MRW4 branch at higher Rayleigh numbers, was traced towards higher Rayleigh numbers beyond its stability range as well. Here we discuss the dynamics for three selected Rayleigh numbers, $Ra = 141$, $Ra = 145$, and $Ra = 165$, which represent distinctive and typical cases on this route. The kinetic energies as functions of time are shown in Fig. 10, while the related power spectra are presented in Fig. 11. In addition, Fig. 12 gives

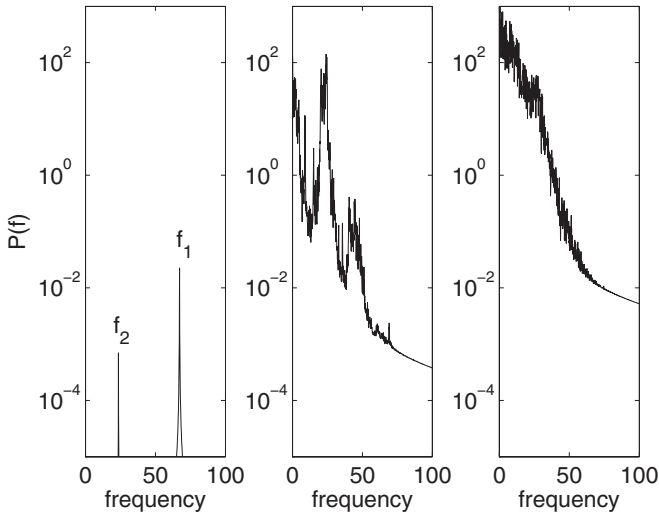


FIG. 11. Power spectrum $P(f)$ of kinetic energy for time-asymptotic states at $Ra = 141$ (left), $Ra = 145$ (middle), and $Ra = 165$ (right) on continuation of the branch MRW3.

the distribution of the kinetic energy over the azimuthal wave numbers for each of the three time-asymptotic states.

Analogously to the MRW4 branch, the MRW3 branch loses stability by the appearance of a further frequency f_2 generating a stable three-frequency solution, as depicted in the top panel of Fig. 10 and the left panel of Fig. 11 for $Ra = 141$. The quasiperiodic or torus solutions decay on further raising the Rayleigh number, leading to aperiodic dynamics. A typical example of the dynamics in this regime, at $Ra = 145$, is presented in the middle panel of Fig. 10 together with the corresponding power spectrum in the middle panel of Fig. 11. The broadening of the original frequency peaks seems to be a typical feature of the torus decay; compare the analogous behavior in the preceding example (the continuation of the MRW4 branch).

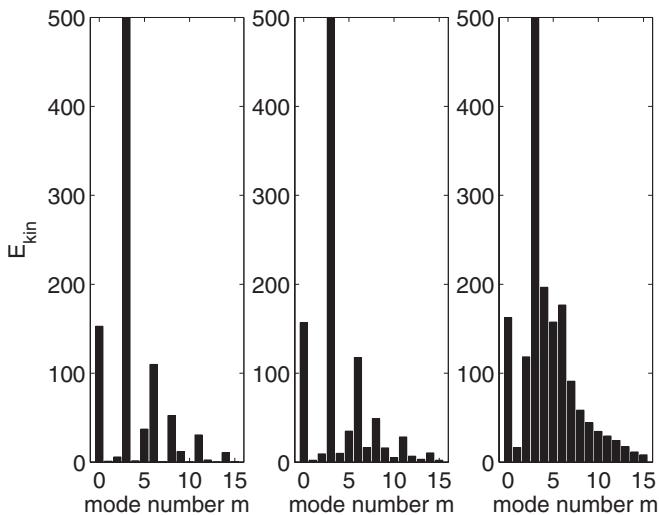


FIG. 12. Distribution of kinetic energy over azimuthal mode number m for time-asymptotic states at $Ra = 141$ (left), $Ra = 145$ (middle), and $Ra = 165$ (right) on continuation of the branch MRW3. The bars for $m = 3$ are cut off at the upper panel margins.

The distribution of the kinetic energy over the wave numbers can be considered as indicative of the degree of complexity of the dynamics. Compared to the rotating wave solution RW3, where only the dominant $m = 3$ mode, its higher harmonics, and the $m = 0$ mode are excited, for the MRW3 solution the $m = 5$ mode is also present. The energy distribution of the subsequent three-frequency solution, shown in the left panel of Fig. 12 for $Ra = 141$, remains qualitatively similar to that of MRW3. In the torus-decay stage which follows, at $Ra = 145$, the distribution remains discrete and almost entirely in these modes, as can be seen in the middle panel of Fig. 12. The excitation of the remaining modes by means of triadic coupling is perceptible, but is still at a low level.

In contrast, at the next stage all of the modes undergo a substantial excitation, as can be seen in the azimuthal wave number distribution in the right panel of Fig. 12 for $Ra = 165$. This wide distribution is obviously related to the complexity of the dynamics seen in the bottom panel of Fig. 10 and to the exponential decay of the frequency spectrum in the right panel of Fig. 11. A question we pose for forthcoming investigations is whether this stage is reached in a continuous process or by an abrupt transition.

For demonstrating chaotic dynamics at high Rayleigh numbers we have used the kinetic energy in the fluid shell, a global quantity. It is of interest, however, to determine whether the chaotic behavior is localized to one or several restricted regions in the shell. We have studied a convective regime at moderate Rayleigh numbers, with the largest scales dominating and smaller scales only weakly excited. The dynamics of our flows may be characterized as weak spatiotemporal chaos in the form of complex oscillations of large-scale structures. Consequently, all spatial regions are involved in the oscillations. The temporal behavior of the radial velocity component at fixed spatial locations shows the same dynamics as the kinetic energy.

VI. DISCUSSION

The purpose of this investigation was to demonstrate the multistability of solutions and their interplay in rotating spherical shell convection. Particular attention was paid to the spatiotemporal features of the solutions, consecutive bifurcations, and the route to chaos. Multistability is primarily manifested in the form of RWs with different fundamental azimuthal wave numbers. All of the RWs we have found in this configuration share the property that they appear with an eastwards (prograde) drift at onset. Furthermore, they show a common linear scaling of the drift rate with the Rayleigh number, and for all of them the drift direction is reversed at some value of the Rayleigh number. We have discussed the transition from prograde to retrograde drift in the context of previous research [12–17].

The property of multistability continues towards higher Rayleigh numbers where all RWs lose stability by Hopf bifurcations in which stable MRWs are generated. We have examined the MRWs resulting from each of the RWs, presenting their wave forms and characterizing them according to the classification of Rand [19].

Some of the MRWs in turn undergo a third Hopf bifurcation, leading to solutions with three clearly identifiable frequencies.

With the examples of the MRW4 and MRW3 branches, we have illustrated the subsequent transitions to transient or permanent chaos, respectively. In summary we state that for higher, but still moderate, Rayleigh numbers, several distinctive solutions of different types exist. Stable MRWs and three-frequency solutions as well as chaotic saddles

and attractors coexist over certain intervals of the Rayleigh number.

ACKNOWLEDGMENT

We wish to thank Udo Schwarz and Antonio Politi for helpful discussions.

-
- [1] S. Chandrasekhar, *Hydrodynamic and Hydromagnetic Stability* (Oxford University Press, New York, 1961).
- [2] P. H. Roberts, *Philos. Trans. R. Soc. London, Ser. A* **263**, 93 (1968).
- [3] F. H. Busse, *J. Fluid Mech.* **44**, 441 (1970).
- [4] G. Geiger and F. H. Busse, *Geophys. Astrophys. Fluid Dyn.* **18**, 147 (1981).
- [5] M. Ardes, F. H. Busse, and J. Wicht, *Phys. Earth Planet Inter.* **99**, 55 (1997).
- [6] R. Simitiev and F. H. Busse, *New J. Phys.* **5**, 97 (2003).
- [7] U. Christensen, J. Aubert, P. Cardin, E. Dormy, S. Gibbons, G. Glatzmaier, E. Grote, Y. Honkura, C. Jones, M. Kono *et al.*, *Phys. Earth Planet. Inter.* **128**, 25 (2001).
- [8] R. Hollerbach, *Int. J. Numer. Methods Fluids* **32**, 773 (2000).
- [9] F. Fedel, K. Bergemann, L. S. Tuckerman, C. Egbers, B. Futterer, M. Gellert, and R. Hollerbach, *Phys. Rev. E* **83**, 046304 (2011).
- [10] E. Knobloch, in *Lectures on Solar and Planetary Dynamos*, edited by M. R. E. Proctor and A. D. Gilbert (Cambridge University Press, Cambridge, 1994), pp. 331–372.
- [11] P. Chossat and R. Lauterbach, *Methods in Equivariant Bifurcations and Dynamical Systems* (World Scientific, Singapore, 2000).
- [12] R. E. Ecke, F. Zhong, and E. Knobloch, *Europhys. Lett.* **19**, 177 (1992).
- [13] K.-K. Zhang and F. H. Busse, *Geophys. Astrophys. Fluid Dyn.* **39**, 119 (1987).
- [14] H. F. Goldstein, E. Knobloch, I. Mercader, and M. Net, *J. Fluid Mech.* **248**, 583 (1993).
- [15] E. Knobloch, *Phys. Fluids* **8**, 1446 (1996).
- [16] L. Li, X. Liao, and K. Zhang, *Phys. Rev. E* **77**, 027301 (2008).
- [17] K. Kimura, S.-I. Takehiro, and M. Yamada, *Phys. Fluids* **23**, 074101 (2011).
- [18] M. Golubitsky and I. Stewart, *The Symmetry Perspective* (Birkhäuser-Verlag, Basel, 2003).
- [19] D. Rand, *Arch. Ration. Mech. Anal.* **79**, 1 (1982).
- [20] M. Gorman and H. L. Swinney, *J. Fluid Mech.* **117**, 123 (1982).
- [21] M. Gorman, H. L. Swinney, and D. A. Rand, *Phys. Rev. Lett.* **46**, 992 (1981).
- [22] M. Golubitsky, V. G. LeBlanc, and I. Melbourne, *J. Nonlinear Sci.* **10**, 69 (2000).
- [23] J. M. Lopez, *J. Fluid Mech.* **553**, 323 (2006).
- [24] Z.-P. Sun, G. Schubert, and G. A. Glatzmaier, *Geophys. Astrophys. Fluid Dyn.* **69**, 95 (1993).